Origin of improved depth penetration in dual-axis optical coherence tomography: a Monte Carlo study

YANG ZHAO, KENGYEH K. CHU, EVAN T. JELLY, AND ADAM WAX1,*

¹Duke University, Biomedical Engineering Department, Durham, NC 27708, USA *Corresponding author: <u>a.wax@duke.edu</u>

Recent studies have demonstrated that extended imaging depth can be achieved using dual-axis optical coherence tomography (DA-OCT). By illuminating and collecting at an oblique angle, multiply forward scattered photons from large probing depths are preferentially detected. However, the mechanism behind the enhancement of imaging depth needs further illumination. Here, the signal of a DA-OCT system is studied using a Monte Carlo (MC) simulation. We modeled light transport in tissue and recorded the spatial and angular distribution of photons exiting the tissue surface. Results indicate that the spatial separation and offset angle created by the non-telecentric scanning configuration promote the collection of more deeply propagating photons than conventional on-axis OCT.

OCIS codes: (110.1650) Coherence imaging; (290.4210) Multiple scattering.

1 Introduction

Optical coherence tomography (OCT) has been widely accepted in the clinical practice of ophthalmology in the diagnosis and management of retinal and choroidal diseases. However, OCT imaging in thick biological tissue remains a challenge. Multiple efforts have been made to improve OCT penetration in tissue. Enhanced depth imaging (EDI) was proposed to balance the falloff of spectral-domain OCT by moving the sample position away from the central (z = 0 mm) region of the image [1, 2]. By inverting the imaging window and placing deep features close to the zero-point, signal attenuation at large probing depths was compensated by the higher sensitivity near the central imaging region. Dynamic focusing is another deep imaging technique that received recent attention. Using this technique, the optical focus of the sample beam is scanned along the axial direction to overcome depth-of-field limitations and maintain high transverse resolution throughout the extended imaging depth [3, 4]. However, neither of these techniques considered the effect of multiple scattering, which fundamentally limits light penetration in tissue.

Optical penetration in biological tissue is limited by multiple scattering. However, scattered photons differ greatly in the amount of useful information they carry. While randomly scattered light creates a diffuse background, multiply forward scattered photons that experience low order scattering events can still carry substantial information and can serve as useful signal [5, 6]. The collection of these multiply forward scattered photons can provide extended imaging depth beyond the ballistic limit [7]. Many optical techniques were designed to utilize multiply forward scattered light, many of which date back long before the invention of OCT. For example, functional near-infrared spectroscopy (fNIRS) was first demonstrated in the late 1970s, in which separate illumination and detection pathways were used to measure cortical oxygenation during hyperventilation [8]. Since then, much of the fNIRS literature reported that the photon trajectories between source-detector pairs exhibit banana-shaped profiles (i.e. deep probing photons have higher probability of travelling further away from illumination along the lateral direction) [9-12].

Spatial offset Raman spectroscopy (SORS) was also designed such that collection was performed at regions spatially offset from the point of incidence. As the collection point is moved further away from the probe beam, the contribution of the spectrum from the deeper layers becomes more apparent. This is because photons generated from greater probing depths are more likely to migrate laterally before being remitted from the sample surface [13, 14].

In the field of low coherence interferometry, a technique called multiple scattering multispectral low coherence interferometry (ms2/LCI) was proposed in early 2010s by our group [7, 15]. The ms2/LCI system utilized separate illumination and collection beams to promote the detection of multiply forward scattered photons. More specifically, the illumination and collection axes

were arranged such that each was at 3-4° relative to normal incidence. This offset between the two axes created both spatial and angular separations between the illumination and collection apertures. The position where the two beams intersect, i.e. the focal zone, is typically placed several mm below tissue surface [15, 16]. Using this dual-axis architecture, photons scattered within the focal zone are favorably detected. This is because there is a low probability of detection for the returning photons that originate outside the focal zone to arrive at the proper location with the correct trajectory to enter the detection aperture. Notably, the dual-axis architecture was first utilized in confocal microscopy to provide better rejection of the out-of-focus background [17]. However, unlike interferometric techniques which use a coherence gate to perform optical sectioning, dual-axis confocal microscopy relies on larger offset angles (~25-30°) and higher NA beams (0.1-0.2) to reject the diffuse background [18-21]. Recently, dual-axis OCT (DA-OCT) was presented as an extension of the previous ms2/LCI method to utilize multiply forward scattered light for deep imaging [22]. The previous ms2/LCI system employed sample translation to enable scanning and thus was limited in imaging throughput. The newly invented DA-OCT system instead utilized a microelectrical-mechanical system (MEMS) mirror to perform beam scanning, which greatly improved the imaging speed while maintaining the dual-axis architecture. We now seek to better elucidate the physical process behind the dual-axis architecture as a means to optimize system performance. We therefore present a MC study which models light-tissue interaction and describes the spatial and angular distribution of photons, from which the deep imaging capability of the DA-OCT system can be explained.

2 Methods

2.1 Definition of Photon Types

G. Yao and L. Wang [23] classified OCT signals into two categories: Class I signal, which refers to light coming from a specific target layer in the medium at a depth that corresponds to the path-length of the reference arm, and Class II signal, which includes light scattered from the rest of the medium above the target layer with its optical path length (OPL) within a coherence length (I_c) of the reference arm path length. Although both Class I and II photons are accepted by the coherence gate, Class I light serves as useful signal while Class II light contributes to an unwanted background and results in the degradation of OCT image contrast.

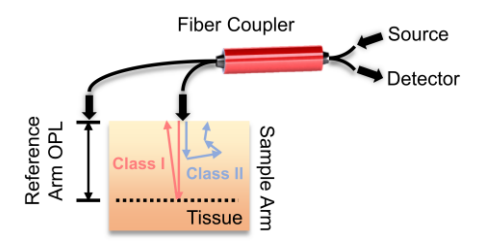


Fig. 1. Class I photons are those coming from a specific target layer in the medium at a depth that corresponds to the path-length of the reference arm and Class II photons are those scattered from the rest of the medium above the target layer with their OPLs within I_c of the reference arm path length.

In our study, we define the optical equivalent penetration (OEP) as one half of the OPL traveled by a photon, and the difference between the OEP and the maximum penetration depth of a photon as the scattering factor (SF):

$$SF = OEP - \max(z) \tag{1}$$

where OEP = OPL / $2n_t$, with n_t as the refractive index of tissue and max(z) is the maximum penetration depth of the photon. A photon with SF close to 0 is ballistic or nearly-ballistic and thus contributes to the conventional OCT signal. In this study, we define photons with SF < l_c as ballistic photons. However, some of these ballistic photons are not truly "ballistic" (i.e. singly scattered), but rather experience a very low number of scattering events yet the excess accumulated path length does not exceed the coherence length. Furthermore, photons that experienced low order scattering events in the forward direction will yield a small SF. Here, we define photons with l_c < SF < $10l_c$ as Class I photons. It has been demonstrated that these minimally scattered photons still carry substantial local tissue information and can serve as useful signal [5, 6]. The information provided by these multiply forward-scattered photons can allow deeper image penetration in tissue, though with a reduction in resolution. In this study, instead of considering these multiply forward-scattered photons as noise, we regard them as Class I signal. Lastly, a photon with a large SF means that the photon experienced multiple scattering with its direction nearly randomized. Therefore, photons with SF > $10l_c$ are classified as Class II photons. The definition of the SF threshold between Class I and Class II photons ($10l_c$ in this study) is highly application dependent. A high SF threshold is preferred in applications where deep imaging is desired and slightly lower resolution can be tolerated. In general, the SF threshold should be determined such that most Class I photons only

experience low order scattering events and still carry local tissue information from the target layer. A more detailed discussion on the SF, including the rationale for selecting 10l_c as the SF threshold in this study, can be found in Section 3.5.

2.2 Preferential Detection of Class I Photons

As probing depth increases in tissue, the intensity of Class II signal increases and gradually overwhelms the Class I signal. Eventually, the Class I and Class II signals can no longer be separated just by the coherence gate. To assess deep tissue information, an enhanced photon rejection mechanism is needed such that Class I signal is preferentially collected and Class II signal is sufficiently suppressed.

Interestingly, Class II photons overwhelm Class I photons at a very shallow depth when integrated across all spatial and angular dimensions. A previous MC study showed that the integrated Class II signal overwhelms Class I signal at a depth <100 μ m in tissue, which potentially could make OCT imaging impossible beyond very shallow depths [23]. Fortunately, the spatial and angular distributions of Class I and II signal are vastly different. Class II signal exhibits a much broader spatial and angular distribution than Class I signal. The finite collection aperture of a conventional coaxial OCT system behaves as an intrinsic spatial gate such that Class I photons are favorably collected over Class II photons. The depth where the intensity of the Class II signal exceeds that of the Class I signal has been defined as the "critical depth" [23]. Calculations of critical depth for a conventional OCT system produced values of approximately 500 μ m (based on assumed properties of the simulated tissue of absorption and scattering coefficients of $\mu_a = 1.5$ cm⁻¹and $\mu_s = 60$ cm⁻¹, refractive index of $n_t = 1.5$, anisotropy of g = 0.9, and coherence length of the light source $l_c = 15$ μ m) [23]. At probing depths beyond 500 μ m, the intensity of Class II signal becomes dominant and the intrinsic spatial gate provided by coaxial OCT fails to provide good image contrast. Therefore, to enable deeper imaging, a better mechanism is needed to reject Class II photons that do not reach the target depths. Our recently developed DA-OCT provides better rejection of out-of-focus photons by utilizing a separate illumination and detection aperture with an dual-axis configuration [22].

2.3 Monte Carlo Simulation of OCT/DA-OCT Signal

The MC code for analyzing DA-OCT signals was designed based on the MC process developed by S. Jacques and L. Wang [24-26]. The customized program was written in MATLAB R2017b (Mathworks, Natick, MA). In this study, we define the offset angle $\Delta\theta$ as the angle between the illumination and collection beams. The illumination/collection angles (angle between the illumination/collection beam and normal incidence) were set equal to half of the offset angle ($\theta_i = \theta_c = \Delta\theta/2$). The illumination beam was simulated as a focused Gaussian beam with a FWHM beam waist of 32 μ m, an incidence angle of $\theta_i = 3^\circ$ ($\Delta\theta = 6^\circ$) with respect to normal incidence (in air) and its focus (z_0) buried 1-3 mm below the tissue surface. The specular reflection from the air-tissue interface was neglected in the simulation. The Henyey-Greenstein phase function was chosen to characterize the scattering angle during the light-tissue interaction [27]. 10^9 incident photons were sampled, and those that exited the tissue surface were analyzed to compare their OPLs with the reference arm path length. A photon was considered accepted by the coherence gate if the difference between the path lengths was less than a coherence length. The MC simulation was performed on a PC equipped with dual Xeon octa-core processors and 24 GB of RAM. Parallel processing (multicore processing) was utilized to speed up the simulation process. The entire simulation took approximately 34 hours.

The lateral distance between the points of incidence and exit as well as the exit angle of a photon at the tissue surface were recorded, which were used to calculate the spatial and angular distribution of the OCT/DA-OCT signal. The optical parameters used in the simulation were chosen to closely match that of a 1300 nm DA-OCT system: the coherence length of the source is l_c = 7.46 μ m; the refractive index of air and tissue are n_a = 1 and n_t = 1.43 respectively. The absorption and scattering coefficient of tissue are μ_a = 1 cm⁻¹ and μ_s = 60 cm⁻¹ respectively. Tissue anisotropy (g) is assumed to be 0.9 unless otherwise noted. More details of the MC calculation process can be found in [24-26].

3 Results

3.1 Spatial Distribution of Class I and II Signal

The spatial distributions of Class I and Class II photons with respect to their maximum probe depths are presented in Fig. 2b and Fig. 2c respectively. Fig. 2b shows the density of Class I photons observed for different spatial offsets between the illumination and collection apertures. The different color lines separate the photons by their maximum probe depth. Due to their negligible contribution, ballistic photons do not appear in this analysis. Similar to previous studies [23], the spatial distribution of Class II signal (Fig 2c) is much broader than that of Class I signal (note the different lateral scale compared to Fig 2b). Although the distribution of both Class I and II signals broaden with probing depth, the Class II signal distribution broadens much faster than that of Class I signal. Therefore, limiting the collection aperture is an effective method for rejecting most of the Class II photons.

The illumination and collection beams are coaxial for a conventional OCT system with no spatial separation between the two beams. Thus, the operating regime of a conventional OCT system (comprising an offset of less than $50 \, \mu m$), indicated by the blue arrow in Fig. 2b is well-suited for the detection of photons with shallow probing depths. However, as illustrated in Fig. 2b, photons with deeper probing depths are more likely to exit the tissue surface further away from the incident position. This result is consistent with previous studies in fNIRS and SORS [13, 14, 28-31]. A schematic plot illustrating the trajectories of OCT and DA-OCT photons is shown in Fig. 2a. From this result, it is clear that spatial separation between the illumination and collection beams should enhance detection of deep photons. Specifically, for a DA-OCT system, the relationship between off-axis angle ($\Delta\theta$), numerical aperture (NA) of the illumination/collection beam, depth of the optical focus under tissue surface (z_0) and spatial separation (Δx) between the illumination and collection beams on the tissue surface is given by:

$$\Delta x \in [(\Delta \theta - 2NA)z_0, (\Delta \theta + 2NA)z_0].$$
 (2)

Based on equation (2), the spatial separations (Δx) of the DA-OCT beams given an off-axis angle ($\Delta \theta$) of 6° are Δx_1 = 60 – 140 μ m, Δx_2 = 130 – 290 μ m and Δx_3 = 195 – 435 μ m for z_0 = 1 mm, 2 mm and 3 mm, respectively. The operating regime of the DA-OCT system was indicated in Fig. 2b for these three penetration depths (indicated by red arrows). As shown, the dual-axis configuration of a DA-OCT system will detect more Class I photons compared to the traditional coaxial OCT arrangement for all OEP depths greater than 200 μ m. Notably, very few shallow Class I photons (200 μ m OEP) were detected far from the illumination beam, which is inevitably the case when the optical focus is placed deep in tissue. Therefore, deep imaging is achieved at the expense of reduced image quality of shallower features. This can be explained by the increase of the effective NA of the combined off-axis beams compared to that of the coaxial beams, resulting in a reduced depth of focus (DOF). A good balance between deep and shallow photon collection is achieved by placing the optical focus roughly 1 mm beneath the surface of tissue. Therefore, we will use Δx_1 = 60 – 140 μ m (corresponding to z_0 = 1 mm) in all the following simulations.

Image contrast is another important measure of image quality which is not only dependent on the signal intensity of Class I photons, but also on the ratio between Class I and Class II photons. Here, we define the signal-to-background ratio (SBR) as the ratio between the number of Class I and Class II photons collected by the imaging system. The SBR of photons with different probing depths were calculated and plotted in Fig. 2d. When the optical focus is placed 1 mm under tissue surface (region with spatial separation of Δx_1 , as noted by the dark red arrow), the DA-OCT system yields a higher SBR than a coaxial OCT system (regions with no or low spatial separation, indicated by the blue arrow) at all probing depths (all line colors). This improvement in SBR is especially pronounced for large probing depths (OEP > 600 μ m, yellow and green lines), where the SBR increased by nearly an order of magnitude compared to the coaxial case. Therefore, the DA-OCT system can provide superior image contrast at depth by spatially separating the illumination and collection beams.

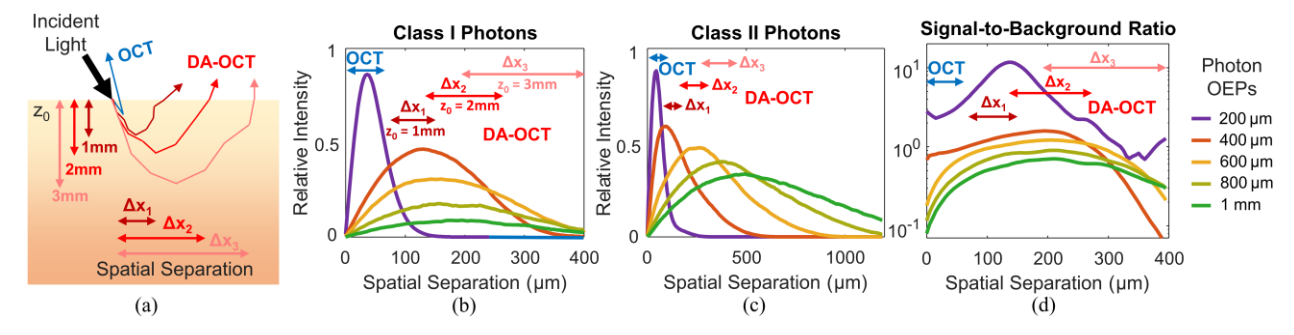


Fig. 2. (a) A schematic plot of OCT and DA-OCT photon trajectories, photons with deeper probing depths are more likely to exit the tissue surface further away from the incident position. (b-c) Spatial distribution of Class I and Class II photons, the different line colors are used to show the optical equivalent penetration (OEP = OPL / $2n_t$, and n_t is the refractive index of tissue) of photons. The blue arrow indicates the region where a conventional coaxial OCT operates, in which photons from shallower depths are mostly collected. The red arrows indicate regions where the DA-OCT operates when the optical focus is placed 1-3 mm under tissue surface. Placing the optical focus deeper into tissue creates larger spatial separation between illumination and detection beams, which favors the collection of deeper photons. (d) SBR of photons with different probing depths. The DA-OCT system provides higher SBR (hence better image contrast) than a coaxial OCT system at nearly all probing depths.

Besides collecting photons that are spatially separated from the illumination beam, the DA-OCT system only collects photons that arrive in the collection aperture within a certain range of angles. This angular gate provides further rejection of Class II photons. Fig. 3a illustrates the angular ranges over which OCT and DA-OCT detect backscattered photons. Fig. 3b-c shows the angular distribution of Class I and II photons exiting the tissue surface when the optical focus was placed $z_0 = 1$ mm under the tissue surface, corresponding to a spatial separation of $\Delta x_1 = 60$ -140 mm and a corresponding angle between illumination and collection, $\Delta\theta$ =6°. The exit angles of Class I photons were mostly distributed between 0-45°, with deeper photons favoring a smaller exit angle. Class II photons, on the other hand, have more uniformly distributed exit angles that spans throughout 0-90°. Although shallower Class I photons (200 and 400 μ m OEPs) exit the tissue at larger angles (10-20°), deeper Class I photons favors smaller exit angles. Thus, by having an offset angle $\Delta\theta$ of approximately 6-8° degrees between the illumination and collection pathways, the DA-OCT system is optimized for the collection of deep Class I photons while suppressing Class II photons. This explains why a half offset angle $\frac{1}{2}\Delta\theta$ of 3-4° provided higher SNR over conventional coaxial OCT under 1 mm tissue-mimicking phantom in our earlier studies [32]. On one hand, a small offset angle (close to 0°) resembles coaxial OCT and provides limited Class II photon rejection capability [15, 16, 32]; on the other hand, a large offset angle reduces the depth of focus of the system, thus degrading the image quality of shallower features. Also, a large angle results in a low photon yield, as very few deep Class I photons exit tissue surface at large exit angles.

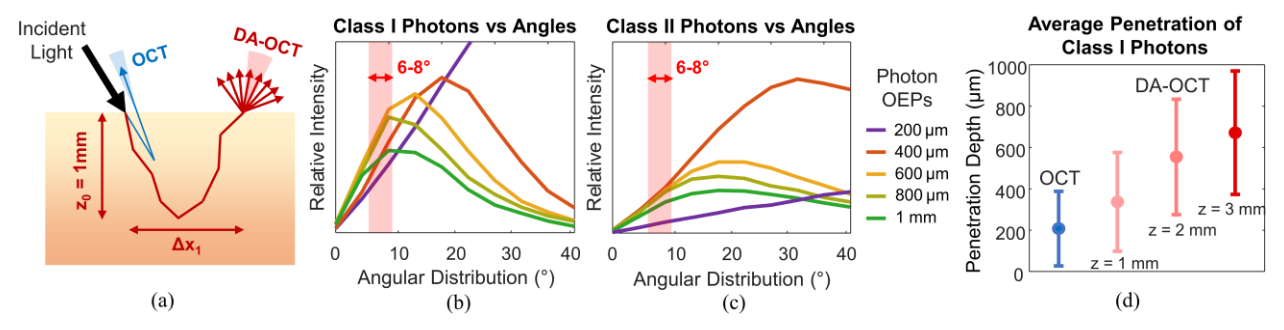


Fig. 3. (a) A schematic plot of the angular ranges of OCT and DA-OCT photon detection. (b-c) Angular distribution of Class I and Class II photons when $z_0 = 1$ mm ($\Delta x \in [60~\mu m, 140~\mu m]$). The blue/red region is where coaxial OCT/DA-OCT operates. Class I photons with deep probing depths favor smaller exit angles, in the 9-20° range. For instance, the exit angles of photons with 1 mm penetration depth peak at ~8°, which is the angular separation between illumination and collection beams of the current DA-OCT system. (d) Average penetration depths of Class I photons collected by OCT and DA-OCT (z_0 = 1, 2 and 3 mm) Error bar: standard deviation of measurements.

3.3 Average Probing Depth of OCT/DA-OCT Signal

The average penetration depths of all the Class I photons collected using OCT and DA-OCT ($z_0 = 1, 2$, and 3 mm) configurations were calculated and are presented in Fig. 3d. As expected, the average photon penetration was greater when the optical focus of the DA-OCT system was placed deeper under the tissue surface. The average probing depths of Class I photons collected by the DA-OCT setup are 374 μ m, 586 μ m and 669 μ m respectively when the optical focus is placed 1, 2 and 3 mm below tissue surface. All of which were greater than those collected by a coaxial OCT system (average probing depth of 205 μ m).

3.4 Image Contrast of DA-OCT

To quantify the image contrast improvement of the DA-OCT system by both spatial and angular rejection of out-of-focus photons, we calculated the SBR of OCT and DA-OCT collected photons, sorted by their probing depths in tissue. Fig. 4a-b shows histograms of the intensity of Class I and Class II signal collected by OCT and DA-OCT systems from the MC simulation. When simulating a coaxial OCT system (Fig. 4a), the signal intensity is high for shallow Class I photons, but the total signal is soon dominated by Class II photons with increasing probing depth. Few Class I photons were detected from greater depths, which led to very low SBR (Fig. 4c). However, more deep Class I photons were collected using the DA-OCT system configuration (Fig. 4b), which generated a significant improvement in SBR. Fig 4c presents the SBR of the OCT and DA-OCT systems with respect to the probing depths. Based on our simulation, the critical depth (where Class II photons begin to exceed Class I signal) of the coaxial OCT is approximately 250 μ m, which is smaller than the 500 μ m reported in [23]. This reduction in critical depth is mainly attributed to our assumption of a focused Gaussian beam with a FWHM beam waist of 32 μ m, rather than a collimated beam with a radius of r_d = 10 μ m, which results in a reduced DOF.. The critical depth of the DA-OCT system under our assumption is nearly 1 mm, a 4-

fold increase compared to the coaxial OCT system. Notably, the SBR of a coaxial OCT system at the same 1 mm probing depth is merely 0.08.

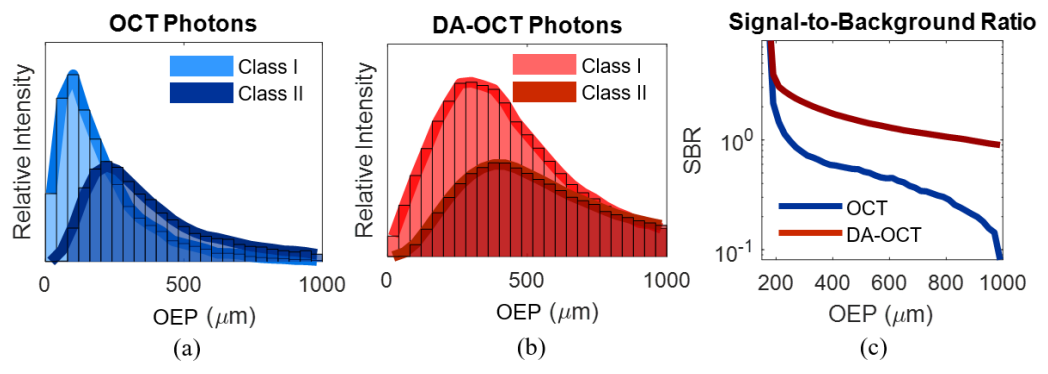


Fig. 4. Histogram of the number of Class I and Class II photons collected by (a) OCT and (b) DA-OCT obtained from the MC simulation, sorted by their OEPs in tissue. (c) The SBR curves obtained under OCT and DA-OCT configurations. The SBR of DA-OCT is much higher than OCT at greater penetration depths. (OEP = OPL / $2n_b$, and n_t is the refractive index of tissue)

3.5 Scattering of Different Photon Types

In this section, we will examine the nature of photons collected by an OCT/DA-OCT system to explain why multiply forward scattered light is preferentially detected by the dual-axis architecture. We first compare the average number of scattering events (sct#) experienced by photons collected from all probing depths using an OCT/DA-OCT system. The DA-OCT system has an offset angle $\Delta\theta$ = 6° and the optical focus is positioned 1 mm below tissue surface. The results are listed in Table 1,

Table 1. Photon scattering events (sct#) collected by an OCT/DA-OCT system.

	Ballistic Photons	Class I Photons	Class II Photons
Conventional OCT	1.67	2.41	6.90
DA-OCT	1.80	3.61	11.92

As shown in Table 1, photons detected by a DA-OCT system experience more scattering events than those collected by a coaxial OCT system, which means that multiply scattered photons are preferentially detected by DA-OCT. For example, Class I photons collected by DA-OCT on average experienced 1.20 (=3.61 – 2.41) more scattering events than those collected by coaxial OCT, while by definition maintaining similar SFs ($I_c < SF < 10I_c$ for Class I photons). Therefore, compared to OCT collected photons, DA-OCT collected photons have experienced more forward scattering events (or, in other words, experienced more low order scattering events).

We can further break down the average scattering number of DA-OCT collected photons by their maximum penetration depths. As shown in Fig. 5, Class II photons with the same penetration depth experience more scattering events than ballistic and Class I photons. With increasing penetration depth, the number of scattering events experienced by Class II photons increases faster than that of ballistic and Class I photons. This can be modeled as a linear relationship for each of the photon types (ballistic, Class I, and Class II),

$$sct = \frac{1}{\beta} \cdot z \tag{3}$$

where z is the maximum penetration depth and sct is the average number of scattering events of a photon. The reciprocal of the linear coefficient in the above equation, β , is an indicator of the difference in average depth penetration between two scattering events. A large β is generally beneficial for deep imaging as it represents a photon having a higher chance of traveling deeper into tissue without losing its forward momentum. Briefly, ballistic photons have the highest momentum in the axial direction and therefore yield the highest β (133 μ m per scattering). The β of Class I and Class II photons depends greatly on the chosen SF threshold. As aforementioned, the SF threshold is the criterion by which a multiply scattered photon is classified as signal (Class I photon) or background (Class II photon). In general, we wish to classify photons that experienced more low order scattering events (i.e. photons with more forward momentum) as Class I photons as they still carry local tissue information from the target layer. Under our current choice of SF_{threshold} = 10Ic, the β of Class I photons (100 μ m per scattering) is within 75% of the β of ballistic light (133 μ m per scattering) and is much higher than that of Class II photons (48 μ m per scattering). This means that the detected Class I photons are indeed highly forward scattered. As presented in an earlier publication, multiply forward scattered (Class I)

photons are useful in probing tissue because their path much more closely resembles that of ballistic light as opposed to diffusely scattered (Class II) light [16].

Fig. 5 also shows that ballistic light (blue line), by our current definition, is not truly ballistic and contains multiply scattered photons even at very shallow depths. The number of scattering events experienced by ballistic light is approximately 2 for 200 μ m and increases to 4 at a depth of roughly 500 μ m. Since these multiply scattered photons still exit the tissue without exceeding the coherence length l_c compared to the length of the reference arm, we suspect that most of these scattering events were lowangle and thus the axial momentum of these photons was mostly preserved.

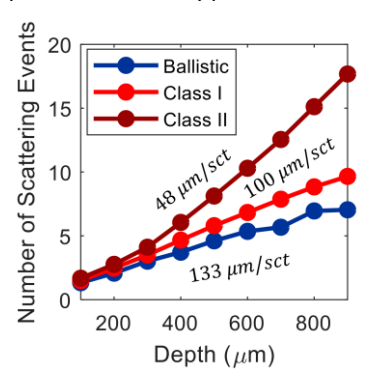


Fig. 5. Number of scattering events of ballistic, Class I and II photons with different penetration depths collected by DA-OCT. The slope of curves in this figure is $1/\beta$ (See Equation (4.3)). The reciprocal of the linear coefficient, β , is an indicator of the amount of depth penetration per scattering event. Class I photons have a similar β compared to ballistic photons, suggesting that they are highly forward scattered. Class II photons, on the other hand, have a much smaller β , suggesting that they have partially lost their forward momentum.

3.6 Effect of Anisotropy on Photon Scattering

Anisotropy (g) is a measure of the amount of forward direction retained after a single scattering event. A biological tissue with a large g value is highly forward scattering. The percentages of ballistic, Class I, and Class II photons collected by our DA-OCT system when interrogating tissues with various anisotropy values are presented in Fig. 6a. Only a very small portion (<1%) of the photons collected by the DA-OCT system were ballistic. The percentage of ballistic photons increased marginally with increasing g (from 0.62% for g = 0.7 to 0.96% for g = 0.95). The percentage of Class I photons, however, increased from 2.92% to 40.7% when g increased from 0.7 to 0.95. This explains why imaging penetration depth is generally deeper in tissue with higher anisotropy (i.e. brain tissue) compared to that with lower anisotropy (i.e. skin tissue). Lastly, the percentage of Class II photons dropped from 2.02% to 2.02% when g increased from 2.02% when g increased from 2.02% when g increased from 2.02% to 2.02% to 2.02% when g increased from 2.02% to 2.02% to 2.02% when g increased from 2.02% to 2.0

Additionally, photons were further grouped based on their maximum penetration depths. Fig. 6b shows the percentages of ballistic, Class I and Class II photons plotted against anisotropy and the maximum penetration depths. The percentage of Class I photons is higher than that of Class II photons for all anisotropy values (g = 0.7 - 0.95) at shallow depths (~100 μ m). However, more scattering events occurred with increasing probing depths and Class I photons were gradually overwhelmed by Class II photons.

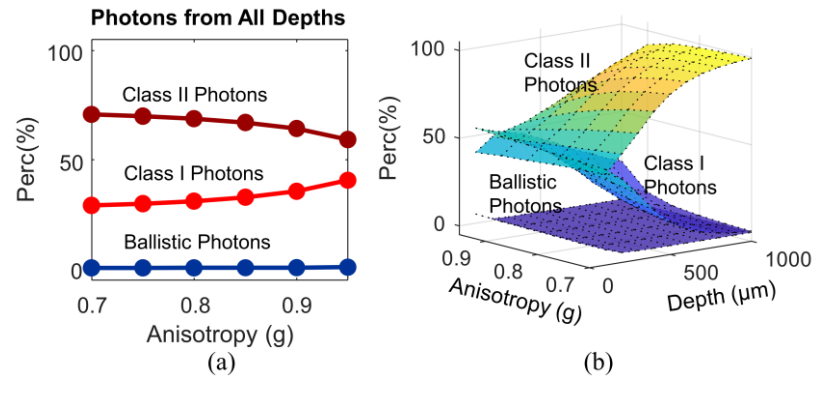


Fig. 6. (a) The percentages of ballistic, Class I and Class II photons collected by the DA-OCT system when examining tissues with various g's. (b) The percentages of ballistic, Class I and Class II photons plotted according to their maximum penetration depths and tissue anisotropy values.

We also studied the effect of anisotropy on the relationship between the number of scattering events and penetration depths of photons. Fig. 7a-b shows the scatter plots of the number of scattering events of DA-OCT collected photons, plotted against their maximum penetration depths for g = 0.7 and 0.95. Given a fixed number of scattering events, photons generally probe deeper in tissue with a higher anisotropy. This trend is especially pronounced for ballistic and Class I photons. The average depth penetration between scattering events is quantified by the parameter β defined in equation (6). A greater β implies a higher chance of deep tissue penetration without losing resolution. The β 's of different photon types in tissue with various anisotropy values were plotted in Fig. 7c. As expected, β is large in tissue with high anisotropy, since photons were highly forward-scattered. Also, ballistic and Class I photons share similar β 's, which were both much higher than that of Class II photons.

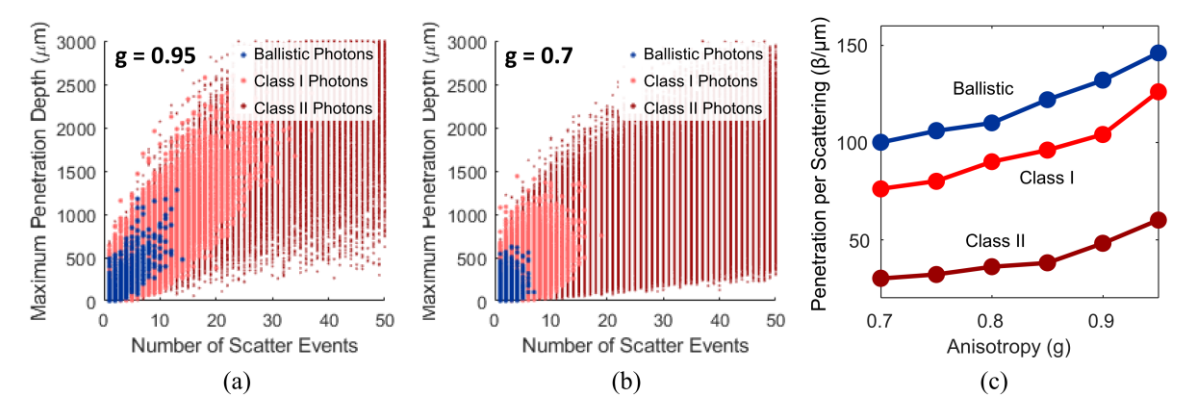


Fig. 7. Number of scattering events by DA-OCT collected photons plotted against their maximum penetration depths for tissue with (a) g = 0.7 and (b) g = 0.95. Tissue with a high anisotropy allows more forward scattering and therefore yields a higher β (average depth penetration between scattering events). (c) β values of tissue with various anisotropy values ranging from 0.7 to 0.95. Ballistic and Class I photons share similar β 's, indicating that Class I photons were highly forward scattered.

4 Conclusions

In this paper, we used a MC method to compare conventional OCT and DA-OCT signal, providing quantitative insight on how the dual-axis architecture promotes deep imaging in tissue. Our MC simulations confirmed that photons with greater probing depths have higher probabilities to exit the tissue surface further away from the incident position. Thus, a non-zero separation between the illumination and collection beam is beneficial for the detection of deep propagating photons. The MC simulations also revealed that deep-propagating Class I photons (desired signal) favor an exit angle between 6-8°, which determined the offset angle of our dual-axis configuration. Therefore, by illuminating and collecting at an oblique angle, the DA-OCT system favors the detection of multiply forward scattered light that propagates through the focal zone (the tissue volume where the illumination and detection beams intersect). Photons scattered outside of the focal zone have much lower probabilities of later taking the proper trajectories to enter the collection aperture. Therefore, DA-OCT offers unique spatial and angular rejection of out-of-focus photons, thus allowing tissue imaging at extended depths. We also calculated the number of scattering events experienced by OCT/DA-OCT photons, as well as the axial penetration depth between successive scattering events. The average number of scattering events (sct#) experienced by DA-OCT collected photons are 1.80, 3.61 and 11.92 for ballistic, Class I and Class II photons respectively, all of which are more than those experienced by photons collected in conventional OCT (sct# = 1.67, 2.41, and 6.90 for ballistic, Class I and Class II photons). To quantify the axial momentum of photons, we defined a term β which captures the axial penetration depth of photons between successive scattering events. Under the assumption of g = 0.9, Class I photons yield $\beta_{\text{class I}} = 100 \, \mu\text{m/sct}$, which is close to that of ballistic photons ($\beta_{\text{ballistic}} = 133 \, \mu\text{m/sct}$) and much larger than that of Class II photons (\(\beta_{class}\) I = 48 \(\mu\)/sct). This means that the photon trajectories of Class I light more closely resemble that of ballistic light as opposed to diffusely scattered (Class II) light, even with a permissive scattering threshold of 10 coherence lengths. DA-OCT is therefore selecting photons that experienced low order scattering events. These highly forward scattered photons still carry substantial local tissue information from the target region. The detection of these photons effectively extends the depth at which interferometric imaging can be performed.

To retrieve precise local tissue information (i.e. if micrometer-level spatial precision is desired), the collection of true ballistic photons (i.e. photons singly scattered from the target region and nowhere else) is needed. However, ballistic photons as defined

by our current convention (photons with SF < I_c) are not truly ballistic and contain multiply scattered photons even at very shallow depths (see Fig. 5). Besides, OCT/DA-OCT systems can never fully eliminate the detection of Class I or Class II scattered photons. This means that the trajectories of photons picked up by OCT/DA-OCT are highly complicated, especially those from deep probing depths. Therefore, extra caution must be taken when extracting localized depth-dependent information (i.e. spectroscopic information) from tissue. This is because the photons that are presumably from the target region may either be from other regions which are shallower than the presumed depth (effect from the Class I/II photons) or have experienced multiple interactions elsewhere along the path to the target region (effect of multiple scattering present in ballistic photons). This implies that spectroscopic OCT (SOCT) may only be reliable when extracting localized information at very shallow depths (where few photons are multiply scattered), or bulk tissue information ("averaged" tissue information of a large region). Extraction of highly localized information of spectroscopic features at extended depths may not be feasible with current SOCT methodology.

In conclusion, our depth-resolved MC study explains why and how the DA-OCT system prioritizes the collection of multiply forward scattered light, thus allowing interferometric imaging at extended depths. The results presented in this paper can be used as a theoretical basis for further development of the DA-OCT system for deep tissue imaging.

References

- 1. R. F. Spaide, H. Koizumi, and M. C. Pozonni, "Enhanced Depth Imaging Spectral-Domain Optical Coherence Tomography," American Journal of Ophthalmology **146**, 496-500 (2008).
- W. J. Brown, S. Kim, and A. Wax, "Noise characterization of supercontinuum sources for low-coherence interferometry applications,"
 J. Opt. Soc. Am. A 31, 2703-2710 (2014).
- 3. W. Drexler, U. Morgner, F. X. Kärtner, C. Pitris, S. A. Boppart, X. D. Li, E. P. Ippen, and J. G. Fujimoto, "In vivo ultrahigh-resolution optical coherence tomography," Opt. Lett. **24**, 1221-1223 (1999).
- 4. Y. Wang, Y. Zhao, J. S. Nelson, Z. Chen, and R. S. Windeler, "Ultrahigh-resolution optical coherence tomography by broadband continuum generation from a photonic crystal fiber," Opt. Lett. 28, 182-184 (2003).
- 5. A. Wax and J. E. Thomas, "Measurement of smoothed Wigner phase-space distributions for small-angle scattering in a turbid medium," J Opt Soc Am A Opt Image Sci Vis 15, 1896-1908 (1998).
- 6. R. K. Wang, "Signal degradation by multiple scattering in optical coherence tomography of dense tissue: a Monte Carlo study towards optical clearing of biotissues," Phys Med Biol **47**, 2281-2299 (2002).
- 7. M. G. Giacomelli and A. Wax, "Imaging beyond the ballistic limit in coherence imaging using multiply scattered light," Opt. Express 19, 4268-4279 (2011).
- 8. F. F. Jobsis, "Noninvasive, Infrared Monitoring of Cerebral and Myocardial Oxygen Sufficiency and Circulatory Parameters," Science 198, 1264-1267 (1977).
- 9. M. Ferrari and V. Quaresima, "A brief review on the history of human functional near-infrared spectroscopy (fNIRS) development and fields of application," NeuroImage **63**, 921-935 (2012).
- 10. P. van der Zee, S. R. Arridge, M. Cope, and D. T. Delpy, "The Effect of Optode Positioning on Optical Pathlength in Near Infrared Spectroscopy of Brain," in *Oxygen Transport to Tissue XII*, J. Piiper, T. K. Goldstick, and M. Meyer, eds. (Springer US, Boston, MA, 1990), pp. 79-84.
- 11. E. Okada, M. Firbank, M. Schweiger, S. R. Arridge, M. Cope, and D. T. Delpy, "Theoretical and experimental investigation of near-infrared light propagation in a model of the adult head," Appl. Opt. **36**, 21-31 (1997).
- 12. M. Soltanlou, M. A. Sitnikova, H.-C. Nuerk, and T. Dresler, "Applications of Functional Near-Infrared Spectroscopy (fNIRS) in Studying Cognitive Development: The Case of Mathematics and Language," Frontiers in Psychology 9(2018).
- 13. P. Matousek, I. P. Clark, E. R. C. Draper, M. D. Morris, A. E. Goodship, N. Everall, M. Towrie, W. F. Finney, and A. W. Parker, "Subsurface Probing in Diffusely Scattering Media Using Spatially Offset Raman Spectroscopy," Appl. Spectrosc. **59**, 393-400 (2005).
- 14. P. Matousek, M. D. Morris, N. Everall, I. P. Clark, M. Towrie, E. Draper, A. Goodship, and A. W. Parker, "Numerical Simulations of Subsurface Probing in Diffusely Scattering Media Using Spatially Offset Raman Spectroscopy," Appl. Spectrosc. **59**, 1485-1492 (2005).
- 15. T. E. Matthews, M. Medina, J. R. Maher, H. Levinson, W. J. Brown, and A. Wax, "Deep tissue imaging using spectroscopic analysis of multiply scattered light," Optica 1, 105-111 (2014).
- 16. T. E. Matthews, M. G. Giacomelli, W. J. Brown, and A. Wax, "Fourier domain multispectral multiple scattering low coherence interferometry," Appl. Opt. **52**, 8220-8228 (2013).
- 17. T. D. Wang, M. J. Mandella, C. H. Contag, and G. S. Kino, "Dual-axis confocal microscope for high-resolution in vivo imaging," Opt. Lett. 28, 414-416 (2003).
- 18. L. K. Wong, M. J. Mandella, G. S. Kino, and T. D. Wang, "Improved rejection of multiply scattered photons in confocal microscopy using dual-axes architecture," Opt. Lett. **32**, 1674-1676 (2007).
- 19. J. T. C. Liu, M. J. Mandella, J. M. Crawford, C. H. Contag, T. D. Wang, and G. S. Kino, "Efficient rejection of scattered light enables deep optical sectioning in turbid media with low-numerical-aperture optics in a dual-axis confocal architecture," J. Biomed. Opt 13, 034020-034021 (2008).
- 20. D. Wang, Y. Chen, Y. Wang, and J. T. C. Liu, "Comparison of line-scanned and point-scanned dual-axis confocal microscope performance," Opt. Lett. **38**, 5280-5283 (2013).
- 21. Y. Chen and J. T. C. Liu, "Optimizing the performance of dual-axis confocal microscopes via Monte-Carlo scattering simulations and diffraction theory," J. Biomed. Opt 18, 066006-066006 (2013).
- 22. Y. Zhao, W. J. Eldridge, J. R. Maher, S. Kim, M. Crose, M. Ibrahim, H. Levinson, and A. Wax, "Dual-axis optical coherence tomography for deep tissue imaging," Opt. Lett. **42**, 2302-2305 (2017).

- 23. Y. Gang and V. W. Lihong, "Monte Carlo simulation of an optical coherence tomography signal in homogeneous turbid media," Physics in Medicine and Biology **44**, 2307 (1999).
- 24. S. L. Jacques, Optical-Thermal Response of Laser-Irradiated Tissue, 2 ed. (Springer Netherlands, 2011), pp. XIV, 958.
- 25. L. Wang and S. L. Jacques, "Optimized radial and angular positions in Monte Carlo modeling," Medical Physics 21, 1081-1083 (1994).
- 26. S. L. Jacques, "Light Distributions from Point, Line and Plane Sources for Photochemical Reactions and Fluorescence in Turbid Biological Tissues," Photochemistry and Photobiology **67**, 23-32 (1998).
- 27. L. J. Steven, "Optical properties of biological tissues: a review," Physics in Medicine and Biology 58, R37 (2013).
- 28. K. W. Calabro and I. J. Bigio, "Influence of the phase function in generalized diffuse reflectance models: review of current formalisms and novel observations," J. Biomed. Opt **19**, 075005-075005 (2014).
- 29. S. C. Feng, F. Zeng, and B. Chance, "Monte Carlo simulations of photon migration path distributions in multiple scattering media," in OE/LASE'93: Optics, Electro-Optics, and Laser Applications in Scienceand Engineering, (SPIE, 1993), 12.
- 30. S. C. Bunce, M. Izzetoglu, K. Izzetoglu, B. Onaral, and K. Pourrezaei, "Functional near-infrared spectroscopy," IEEE Engineering in Medicine and Biology Magazine 25, 54-62 (2006).
- 31. A. Lev and B. G. Sfez, "Direct, noninvasive detection of photon density in turbid media," Opt. Lett. 27, 473-475 (2002).
- 32. Y. Zhao, J. R. Maher, M. M. Ibrahim, J. S. Chien, H. Levinson, and A. Wax, "Deep imaging of absorption and scattering features by multispectral multiple scattering low coherence interferometry," Biomed. Opt. Express 7, 3916-3926 (2016).